

# We are IntechOpen, the world's leading publisher of Open Access books Built by scientists, for scientists

6,900

Open access books available

186,000

International authors and editors

200M

Downloads

Our authors are among the

154

Countries delivered to

TOP 1%

most cited scientists

12.2%

Contributors from top 500 universities



WEB OF SCIENCE™

Selection of our books indexed in the Book Citation Index  
in Web of Science™ Core Collection (BKCI)

Interested in publishing with us?  
Contact [book.department@intechopen.com](mailto:book.department@intechopen.com)

Numbers displayed above are based on latest data collected.  
For more information visit [www.intechopen.com](http://www.intechopen.com)



---

# Ultrafast Dynamics in Topological Insulators

---

Phuoc Huu Le and Chih-Wei Luo

Additional information is available at the end of the chapter

<http://dx.doi.org/10.5772/intechopen.74918>

---

## Abstract

Ultrafast dynamics of carriers and phonons in topological insulator  $\text{Bi}_2\text{Se}_3$ ,  $\text{Cu}_x\text{Bi}_2\text{Se}_3$  ( $x = 0, 0.1, 0.125$ ) single crystals were studied by time-resolved pump-probe spectroscopy. The coherent optical phonon ( $A_{1g}^{-1}$ ) is found via the damped oscillation in the transient reflectivity changes ( $\Delta R/R$ ) for  $\text{Cu}_x\text{Bi}_2\text{Se}_3$ . The observed red shift of  $A_{1g}^{-1}$  phonon frequency suggests the intercalation of Cu atoms between a pair of the quintuple layers of  $\text{Bi}_2\text{Se}_3$  crystals. Moreover, the relaxation processes of Dirac fermion near the Dirac point of  $\text{Bi}_2\text{Se}_3$  are studied by optical pump and mid-infrared probe spectroscopy through analyzing the negative peak of the  $\Delta R/R$ . The Dirac fermion-phonon coupling strength was found in the range of 0.08–0.19 and the strength is reduced as it gets closer to the Dirac point. The ultrafast dynamics and fundamental parameters revealed by time-resolved pump-probe spectroscopy are important for designing the optoelectronics in the mid-IR and THz ranges.

**Keywords:** topological insulators, ultrafast dynamics, pump-probe spectroscopy, Dirac fermion

---

## 1. Introduction

Recently, topological insulators (TIs) [1–8] and two-dimensional (2D) materials such as graphene [9],  $\text{MoS}_2$ ,  $\text{WS}_2$ , and  $\text{MoSe}_2$  [10] are of great interests because of their unique physical properties and applications. These materials have a band structure that is linearly dispersed with respect to momentum, in which the transportation of electrons in these materials is essentially governed by Dirac's (relativistic) equation with zero rest mass and an effective "speed of light" —  $c^* \approx 10^6$  m/s [9]. In TIs, a novel electronic state called the topological surface state (TSS) has been predicted and observed [1–8]. Unlike the trivial insulator, TIs have a spin degenerate and fully gapped bulk state but exhibit a spin polarized and gapless electronic state on the surface [8]. This metallic surface state has a linear energy-momentum dispersion

---

relation in the low-energy region, which is known as a Dirac cone. Unlike the Dirac cone of graphene, the Dirac cone of a TI is protected by the time-reversal symmetry. This robust TSS can survive under time-reversal invariant perturbations, such as surface pollution, crystalline defects, and distortions of the surface [6]. Additionally, because of the fully spin-polarized characteristics of the surface state, TIs have a high potential for the development of spintronic devices and quantum computation [6, 11].

The optoelectronic properties of TIs are important subjects for the development of optoelectronic devices. Therefore, the issues associated with electron–phonon interaction, carrier lifetime, carrier dynamics, energy loss rate, and low-energy electronic responses are very important for optimizing device performance. These ultrafast dynamic properties of the materials can be resolved by pump-probe spectroscopy. This chapter provides a brief introduction to the materials, time-resolved pump-probe spectroscopy, and some ultrafast dynamic properties of Bi-based topological insulators.

## 2. Bismuth-based topological insulators

Bismuth chalcogenide compounds ( $\text{Bi}_2\text{Ch}_3$ , Ch = Se, Te) have been extensively investigated in material science and condensed-matter physics because of their intriguing properties regarding thermoelectricity [12–14] and three-dimensional TIs [15–18].  $\text{Bi}_2\text{Ch}_3$  is a narrow bandgap semiconductor with a rhombohedral crystal structure belonging to the  $D_{3d}^5(R\bar{3}m)$  space group. The  $\text{Bi}_2\text{Ch}_3$  crystal structure is constructed from repeated quintuple layers (QLs) arranged along the  $c$ -axis. The unit lattice cell of a  $\text{Bi}_2\text{Ch}_3$  crystal is composed of three QLs. Each QL is stacked in a sequence of atomic layers Ch(1)-Bi-Ch(2)-Bi-Ch(1) and is weakly bonded to the next QL via Van der Waals interaction. The crystal structures of  $\text{Bi}_2\text{Se}_3$  and  $\text{Bi}_2\text{Te}_3$  are shown in **Figure 1**. For convenience, these crystal structures are also described by a hexagonal lattice, where the  $a$ -axis and  $c$ -axis lattice constants of  $\text{Bi}_2\text{Se}_3$  ( $\text{Bi}_2\text{Te}_3$ ) are 4.138 Å (4.384 Å) and 28.64 Å (30.487 Å), respectively [19].

In 2009, Zhang et al. predicted that the  $\text{Bi}_2\text{Ch}_3$  crystal is a strong TI [15]. A calculation of the electronic structure with spin-orbit coupling in the  $\text{Bi}_2\text{Se}_3$  crystal has also been performed [15]. By tuning the spin-orbit coupling in the system, band inversion occurred around the  $\Gamma$  point. As these two levels, which are closest to the Fermi energy, have opposite parity, the inversion between them drives the system into a TI phase [15]. **Figure 2** shows the calculated energy and momentum dependence of the local density of states (LDOS) for  $\text{Sb}_2\text{Se}_3$ ,  $\text{Sb}_2\text{Te}_3$ ,  $\text{Bi}_2\text{Se}_3$ , and  $\text{Bi}_2\text{Te}_3$ . All of these materials have the same rhombohedral crystal structure with the space group  $D_{3d}^5(R\bar{3}m)$ . Zhang et al. predicted that  $\text{Bi}_2\text{Se}_3$ ,  $\text{Bi}_2\text{Te}_3$ , and  $\text{Sb}_2\text{Se}_3$  are candidates for a TI, whereas  $\text{Sb}_2\text{Te}_3$  is not because the spin-orbit coupling effect of  $\text{Sb}_2\text{Te}_3$  is not strong enough to induce band inversion [15]. Following this prediction, Xia et al. [20] and Hsieh et al. [4] investigated the existence of the TSS in  $\text{Bi}_2\text{Se}_3$ ,  $\text{Bi}_2\text{Te}_3$ , and  $\text{Sb}_2\text{Se}_3$  through angle-resolved photoemission spectroscopy (ARPES).

**Figure 3(a)** and **(b)** shows the ARPES results of the surface electronic structure on a  $\text{Bi}_2\text{Se}_3$  (111) surface [20]. Around the  $\bar{\Gamma}$  point, the clear V-shaped band is observed to approach the

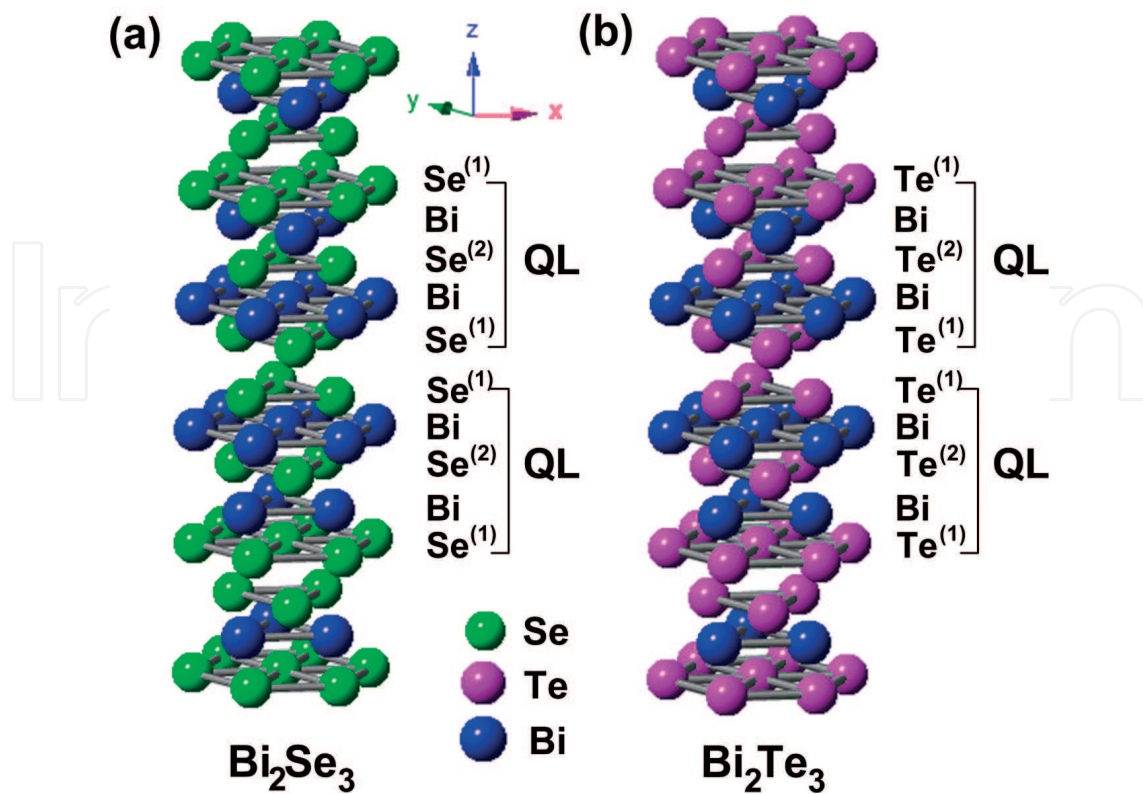


**Figure 1.** (a) The crystal structures of (a)  $\text{Bi}_2\text{Se}_3$  and (b)  $\text{Bi}_2\text{Te}_3$ , in which 5-atomic-layer-thick lamellae of  $-(\text{Se}^{(1)}-\text{Bi}-\text{Se}^{(2)}-\text{Bi}-\text{Se}^{(1)})-$  or  $-(\text{Te}^{(1)}-\text{Bi}-\text{Te}^{(2)}-\text{Bi}-\text{Te}^{(1)})-$  is called a quintuple layer (QL).

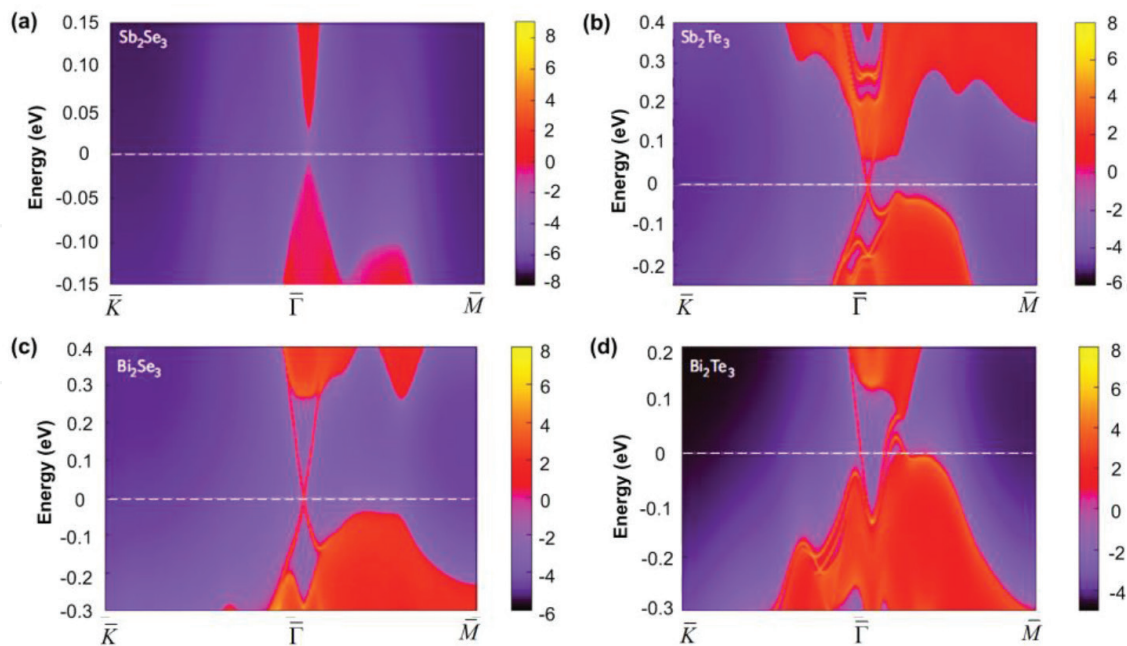


**Figure 2.** The calculated energy and momentum dependence of the LDOS for (a)  $\text{Sb}_2\text{Se}_3$ , (b)  $\text{Sb}_2\text{Te}_3$ , (c)  $\text{Bi}_2\text{Se}_3$ , and (d)  $\text{Bi}_2\text{Te}_3$  on the (111) surface. The TSSs are clearly seen around the  $\Gamma$  point as a red line in the  $\text{Sb}_2\text{Te}_3$ ,  $\text{Bi}_2\text{Se}_3$ , and  $\text{Bi}_2\text{Te}_3$  graphs. No TSS exists in  $\text{Sb}_2\text{Se}_3$  [15].

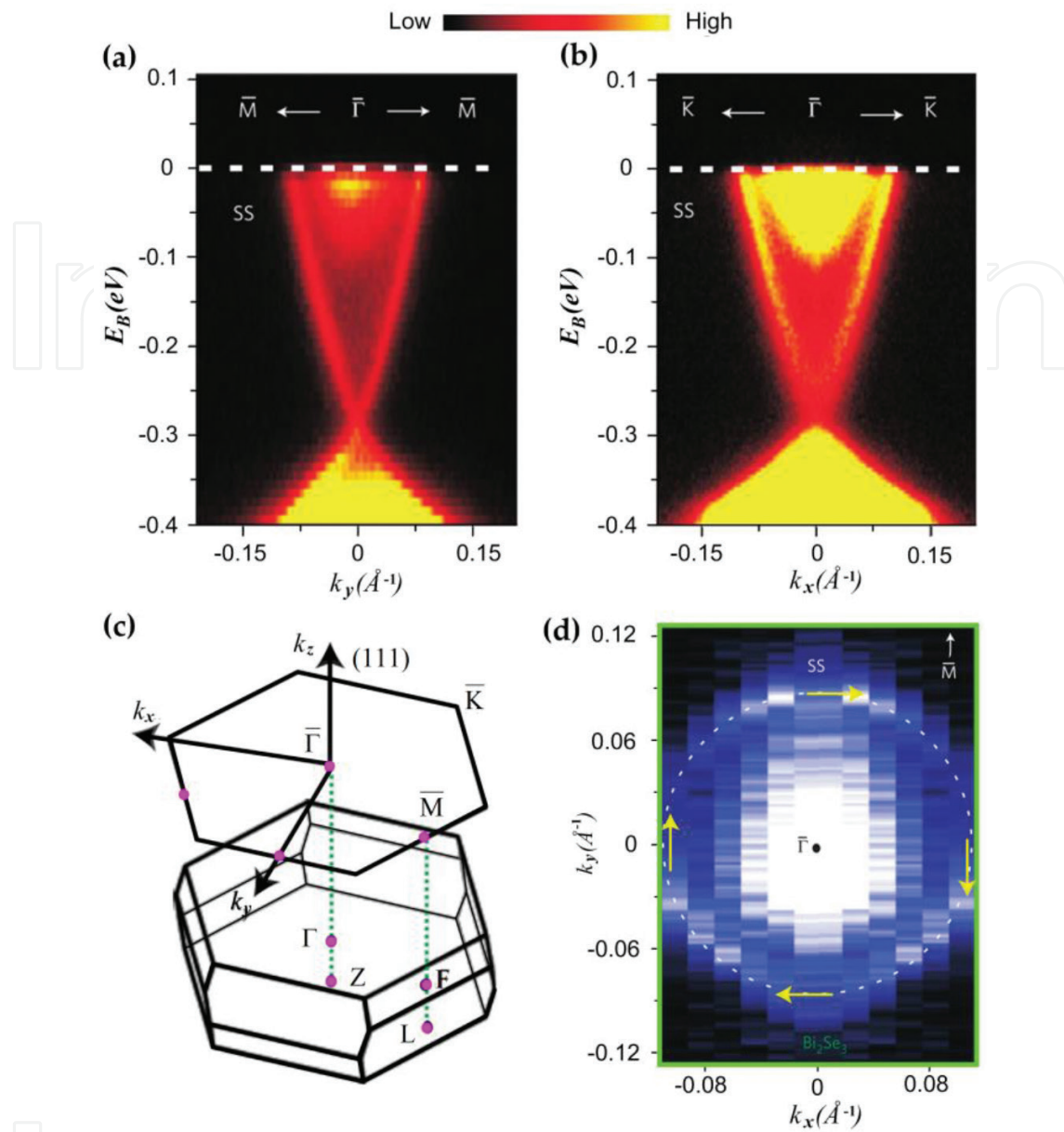


**Figure 3.** The ARPES measurements of the electronic structure on  $\text{Bi}_2\text{Se}_3$  near the  $\bar{\Gamma}$  point along the (a)  $\bar{\Gamma}-\bar{M}$  and (b)  $\bar{\Gamma}-\bar{K}$  directions. (c) The bulk 3D Brillouin zone and the surface 2D Brillouin zone of the projected (111) surface. (d) The Fermi surface of the surface state [20].

Fermi level. The slopes of this V-shaped band along the  $\bar{\Gamma}-\bar{M}$  and  $\bar{\Gamma}-\bar{K}$  directions are nearly equivalent [20]. The U-shaped bands near the Fermi level and below the V-shaped band are the bulk conduction band (BCB) and bulk valence band (BVB) of  $\text{Bi}_2\text{Se}_3$ . This result matches the prediction that the surface state exists between the BCB and the BVB. The detail of the surface state is shown in **Figure 3(d)**. The ring-like Fermi surface formed by the Dirac cone-like surface state is centered at the  $\bar{\Gamma}$  point. The unique spin-momentum lock behavior can also be observed in this figure.

### 3. Principle of femtosecond spectroscopy

#### 3.1. Degenerate pump-probe spectroscopy

Highly temporal resolution is one of the unique characteristics in femtosecond optics. By the pump-probe technique, the photoexcited carrier dynamics and phonon dynamics in solid state materials can be clearly resolved. Additionally, the interband and intraband relaxation processes can be also obtained.

The basic understanding of time-resolved pump-probe spectroscopy is introduced as follows. The pump pulses are served as a perturbation which leads to the changes of the electronic population in materials. The probe pulses are used for the detection of the optical property changes of the materials. By controlling the time interval between the pump and probe pulses, the transient changes of the optical properties can be recorded. In pump-probe spectroscopies, the transient reflectivity changes ( $\Delta R/R$ ) or transient absorption changes ( $\Delta A/A$ ) can be measured.

Here, we explain more experimental details about the detection of  $\Delta R/R$ . As shown in **Figure 4**, the pump-induced reflectivity changes are plotted as  $R(t)$ . The  $f_{\text{modulation}}$  is the modulation frequency of the chopper. The  $f_{\text{laser}}$  is the repetition rate of femtosecond laser pluses. The period of the  $R(t)$  is correlating to the period of the  $I_{\text{pump}}(t)$  pulse train. Since the reflectivity of material,  $R(t)$ , is modulated by the  $I_{\text{pump}}(t)$  pulse train, the intensity of reflective probe beam  $I_{R,\text{probe}}(t)$  is also modulated by the  $I_{\text{pump}}(t)$  pulse train. Thus, the  $I_{R,\text{probe}}(t)$  can be described by the superposition of the DC intensity signal  $I_{R,0}$  and AC intensity signal  $\Delta I_R$  with the specific frequency  $f (= f_{\text{modulation}})$ . Typically, the  $\Delta I_R$  is much smaller than the  $I_{R,0}$  in the order of  $10^{-3}$ – $10^{-6}$ . By using the phase-lock technique, the amplitude of AC intensity signal  $\Delta I_R$  can be extracted out by providing the reference frequency  $f_{\text{modulation}}$  for the lock-in amplifier. Because the  $\Delta I_R$  is small compared to the  $I_{R,0}$ , the  $\langle I_{R,\text{probe}}(t) \rangle = I_{R,0} + \Delta I_R/2 \approx I_{R,0}$ . Thus, the  $I_{R,0}$  can be obtained by using a multimeter for the measurements of  $\langle I_{R,\text{probe}}(t) \rangle$ . The measured  $\Delta R/R$  can directly relate to the  $\Delta I_R/I_{R,0}$  via the following relationship.

$$\frac{\Delta R}{R} = \frac{\Delta I_R/I_{i,\text{probe}}}{I_{R,0}/I_{i,\text{probe}}} = \frac{\Delta I_R}{I_{R,0}} \quad (1)$$

where the  $I_{i,\text{probe}}$  is the intensity of the incident probe beam. Thus, the time evolution of  $\Delta R(t)/R$  can be measured by swapping the time interval  $\Delta t$  between the pump pulse and the probe pulse.

#### 3.2. Optical pump and mid-infrared probe spectroscopy

The plasma edge of the doped n-type semiconductor usually lies in the mid-infrared (MIR) regime. By measuring the reflectivity around the plasma edge, many characteristics of carriers such as scattering rate and carrier concentration can be obtained [21]. The development of a pulsed mid-infrared light source provides the opportunities for understanding the dynamics of carriers. The mid-infrared pump-probe spectroscopy has been already applied on various

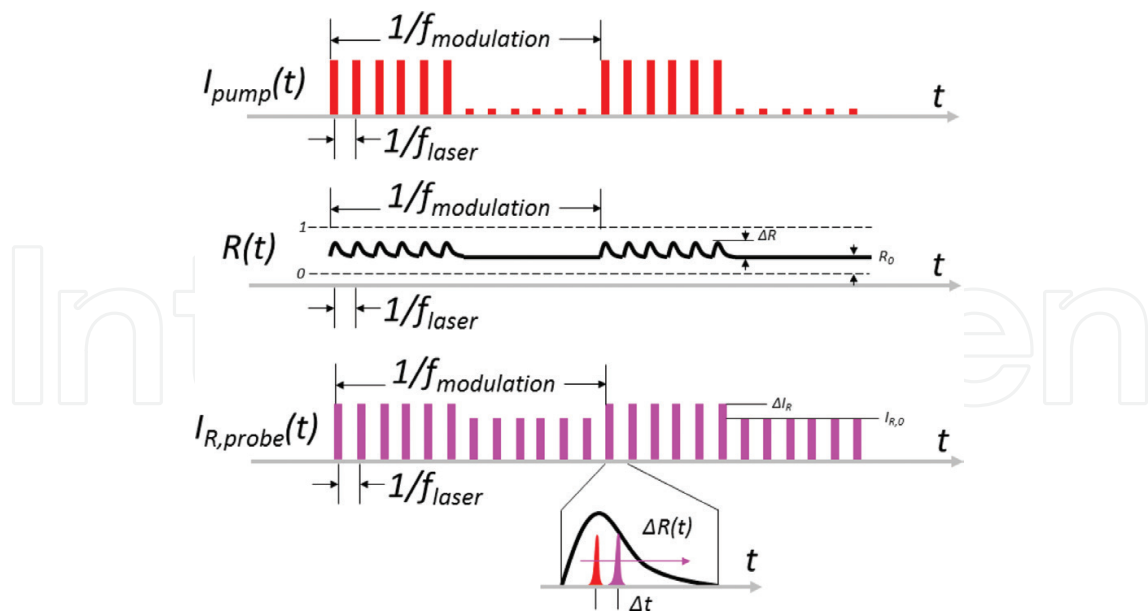


**Figure 4.** The scheme for the principle of the pump-probe technique. The details are described in the text.

materials (i.e., oxides, semiconductors, superconductors, graphene, and topological insulators) [22–28]. In the reflection-type mid-infrared pump-probe spectroscopy, the effect of multiple reflections should be considered in the analysis, and the dynamical characteristics of carriers can be further obtained through modeling the measured data with the Drude-Lorentz model.

**Figure 5** shows a schematic diagram of our optical pump and mid-infrared probe (OPMP) spectroscopy. The light source of the pump-probe system is a regenerative amplifier with 800 nm

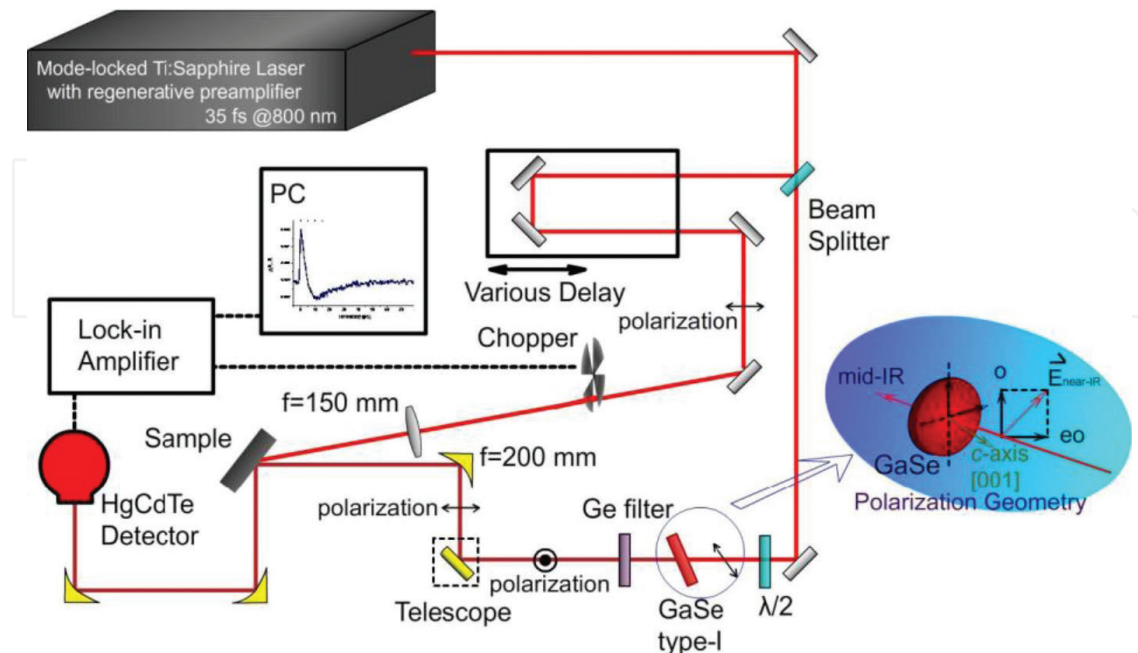


**Figure 5.** Schematic diagram of the optical pump and mid-infrared probe (OPMP) system.

central wavelength, 5 kHz repetition rate, and 30 fs pulse duration. The beam is split into a pump beam (40% of the incident light) and a probe beam (60% of the incident light). The probe beam passes through a 0.7-mm-thick GaSe crystal to generate mid-infrared (MIR) pulses, in which the MIR wavelength can be tuned from 9.0  $\mu\text{m}$  (138 meV) to 14.1  $\mu\text{m}$  (88 meV) through differential frequency generation (DFG). The optical pump beam with the fluence of 68  $\mu\text{J}/\text{cm}^2$  and a spot size of 485  $\mu\text{m}$  (in diameter) is focused on the sample using a 150 mm lens. An Au-coated off-axis parabolic mirror with  $f = 200$  mm is employed to focus the probe beam on the sample surface with a spot diameter of 392  $\mu\text{m}$ . It is ensured that the spot size of the pump beam is larger than that of the probe beam. The probe beam is further collimated and refocused onto a MIR detector (e.g., liquid nitrogen-cooled HgCdTe) using an Au-coated off-axis parabolic mirror ( $f = 50$  mm).

## 4. Ultrafast dynamics in topological insulators

### 4.1. Time-resolved spectroscopy in a topological insulators

The dynamic properties of photoexcited TIs have attracted a great deal of attention. For example, the relaxation behavior of a carrier near the Fermi surface has been observed by the time-resolved angle-resolved photoemission spectroscopy (Tr-ARPES) [29–32]. **Figure 6(c)** shows that the 1.55 eV photons excite the electrons from the bulk valence band to a higher-lying state in the bulk materials. Then, the photoexcited carriers fall into the bulk conduction band (BCB) and the surface state within 1 ps [31]. In **Figure 6(a)**, we can see the rise time of curve 10 is  $\sim 1$  ps. This means that after photoexcitation, the carriers in the higher lying band are rapidly relaxed into the BCB, then cooled to the bottom of the BCB via intraband scattering. These interband transitions and intraband scattering are shown in **Figure 6(d)** and **(e)** [31].

Furthermore, the relaxation time of curve 10 in **Figure 6(a)** is longer than 10 ps. This slow relaxation indicates the metastable behavior of the population of carriers in the BCB [30, 31]. Meanwhile, as curves 6–9 shown in **Figure 6(b)**, the population of surface states also exhibits an unusually long-lived existence [31]. Here, the relaxation bottleneck is attributed to the scattering processes between the BCB and the surface state [31]. As **Figure 6(f)** shows, the photoexcited carriers first relax via surface-bulk scattering and then cooling via surface-state intraband scattering. This scattering channel is mainly in response to the acoustic phonon-mediated surface-bulk coupling and the acoustic phonon scattering of the surface-state Dirac fermions [32]. The Tr-ARPES can directly deliver information about the population changes of the electronic state near the Fermi level. However, reports on the transition processes occurring in the early stages after photoexcitation are rare. To fully understand the photoexcited carrier dynamics, studies for the interband transition and the intraband cooling are needed, which can be revealed using optical pump/optical probe spectroscopy (OPOP) and optical-pump/mid-infrared probe (OPMP) spectroscopy.

### 4.2. Interband relaxations in topological insulators

The interband relaxation of photoexcited carriers in topological insulator (TI) single crystals is examined by the optical pump and optical probe spectroscopy [33]. In this section, we present the phonon and carrier dynamics in doped TI  $\text{Cu}_x\text{Bi}_2\text{Se}_3$  ( $x = 0, 0.1, 0.125$ ) single crystals.

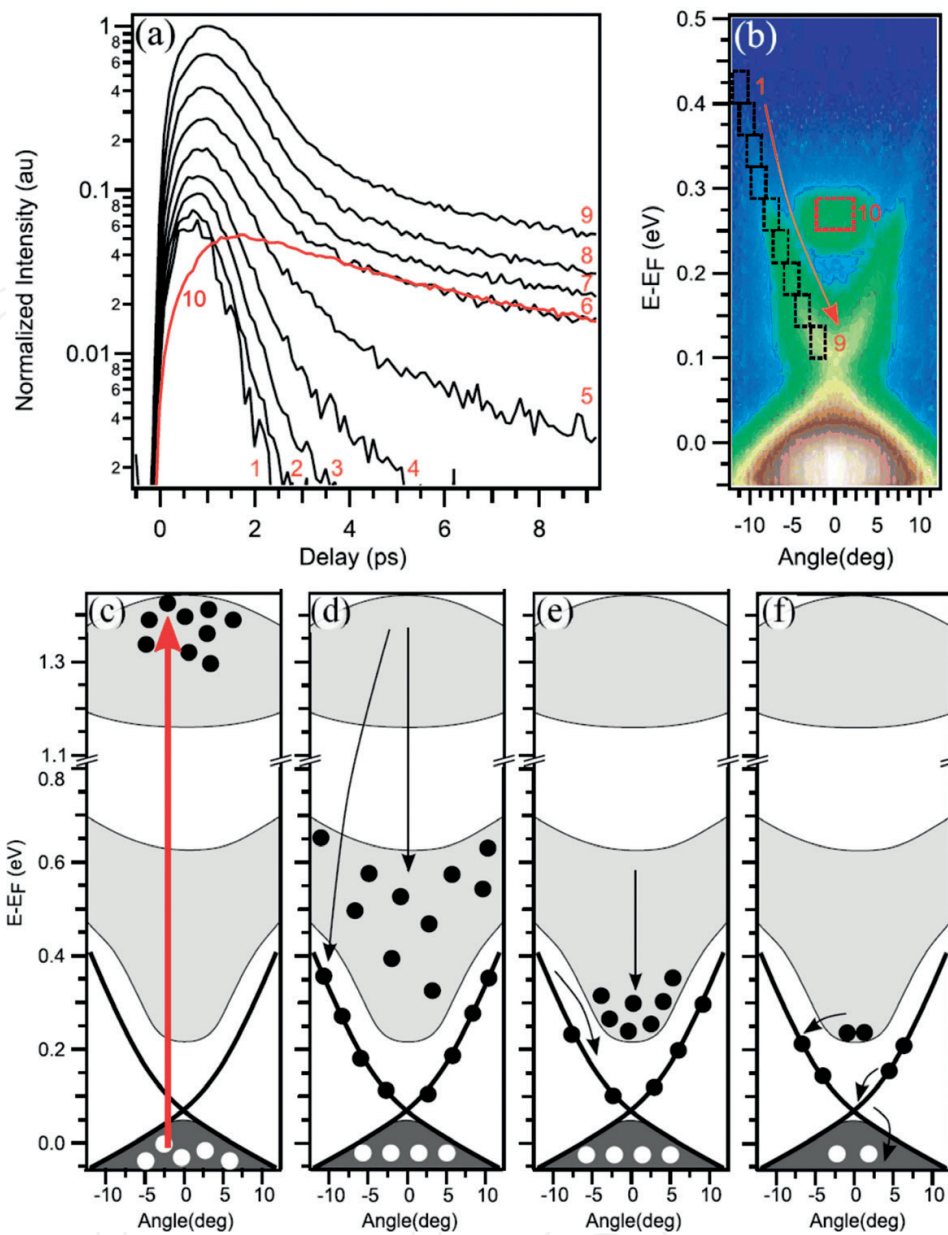


**Figure 6.** (a) The normalized population within the integration windows indicated in (b). (b) The integration windows over the BCB and the surface state. (c)–(f) Schematics of carrier dynamics over the transition energy range [31]. (c)  $t = 0$  ps. (d)  $t \sim 0.5$  ps. (e)  $t \sim 2.5$  ps. (f)  $t > 5$  ps.

**Figure 7(a)** shows the typical  $\Delta R/R$  signals as a function of delay time for  $\text{Cu}_x\text{Bi}_2\text{Se}_3$  crystals at room temperature. Generally, different energy-transfer processes can be unambiguously extracted from the time evolution of  $\Delta R/R$  curve. After pumping, the thermalization between electrons and optical phonons which occurred in a sub-picosecond timescale is characterized by the fast component in  $\Delta R/R$ . A subsequent slow component in a timescale of several picoseconds is assigned to the thermalization between electrons and acoustic phonons [34]. After these electron-lattice relaxation processes, the heat diffusion out of the illuminated area on the sample is further revealed by the quasi-constant component in  $\Delta R/R$  [35]. Furthermore, all of the  $\Delta R/R$  curves show two damped oscillation components with different periods.

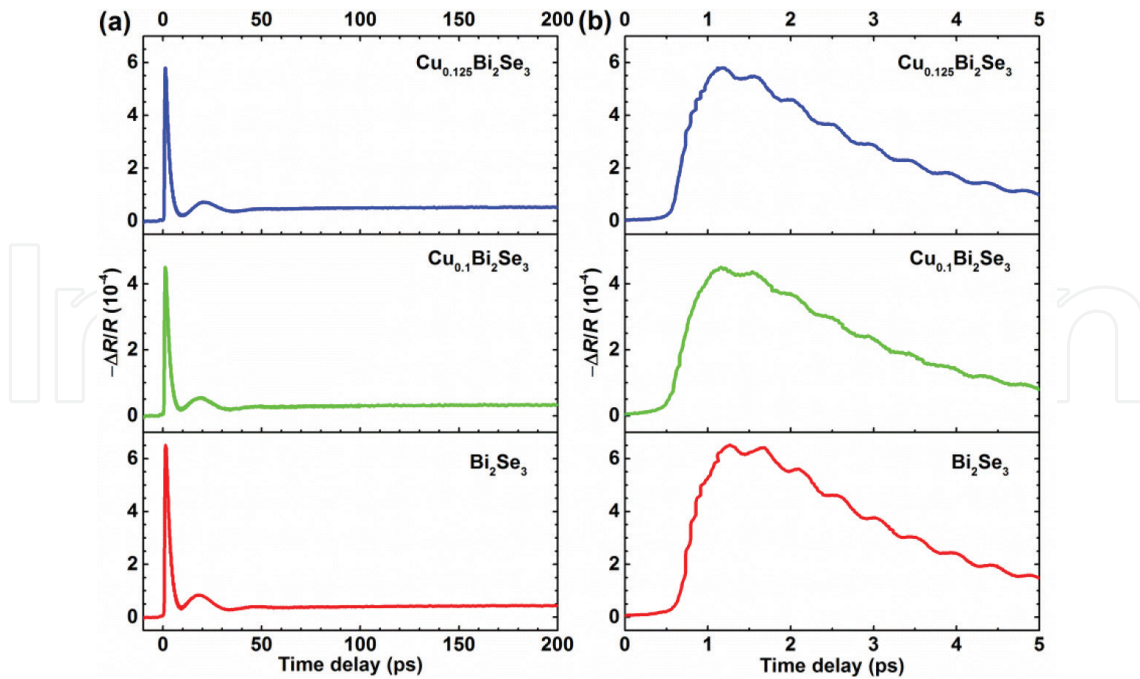


**Figure 7.** Temporal variations of  $\Delta R/R$  signals for  $\text{Cu}_x\text{Bi}_2\text{Se}_3$  crystals ( $x = 0, 0.1, 0.125$ ) at room temperature by using the 1.55 eV degenerate pump-probe spectroscopy, shown (a) in the full timescale and (b) in short timescale.

The slow oscillation components, as shown in **Figure 7(a)**, are attributed to the coherent acoustic phonons (CAPs) generated by ultrafast laser pulses. This damped slow oscillation in  $\Delta R/R$  is generated by the interference between two probe beams, respectively, reflected from the sample surface and the strain pulse that propagate longitudinally with the sound velocity. The relationship between the period  $\tau_{\text{CAP}}$  of the slow oscillation and the longitudinal sound velocity  $v_s$  is  $\tau_{\text{CAP}} = \lambda / (v_s \sqrt{n^2 - \sin^2 \theta})$ , where  $\lambda$  is the probe wavelength,  $n$  is the refractive index at  $\lambda$ , and  $\theta$  is the incident angle of the probe beam [33]. Consequently, the sound velocity can be estimated by measuring the CAP oscillations when the refractive index of the material is known. The frequency of the CAP for the  $\text{Bi}_2\text{Se}_3$  crystals is  $\sim 0.033$  THz ( $\sim 30$  ps in period). Additionally, it completely decays within  $\sim 60$  ps. The disappearance of the CAP (slow oscillation) around 60 ps, according to the strain pulse model, is determined by the penetration depth of an 800 nm probe beam in  $\text{Bi}_2\text{Se}_3$  crystals. Taking the refractive index of  $\text{Bi}_2\text{Se}_3$  crystals reported in [36], the sound velocity is estimated to be 1996 m/s at room temperature [33]. **Figure 7(a)** also reveals that the periods of the slow oscillations in  $\text{Cu}_x\text{Bi}_2\text{Se}_3$  ( $x = 0, 0.1, 0.125$ ) crystals vary slightly from 29.9 to 30.2 ps.

The fast oscillation components of  $\text{Cu}_x\text{Bi}_2\text{Se}_3$  crystals are presented in **Figure 7(b)**, which can be extracted by removing the relaxation background from the  $\Delta R/R$  signals. The results are presented in **Figure 8(a)**. The frequency of the component is 2.148 THz, which can be further assigned as the  $A_{1g}^{-1}$  coherent optical phonon (COP) mode of  $\text{Bi}_2\text{Se}_3$ , based on comparison with the steady-state Raman spectroscopy [37]. Interestingly, the frequencies of the fast oscillations considerably vary with Cu content ( $x$ ) of the  $\text{Cu}_x\text{Bi}_2\text{Se}_3$  samples and are associated with the changes in the chain length of the QL and in the lattice constant of  $c$ -axis.

**Figure 8(a)** shows the fast oscillation component for  $\text{Cu}_x\text{Bi}_2\text{Se}_3$  ( $x = 0, 0.1, 0.125$ ) crystals. In order to quantitatively analyze these oscillations, a damped oscillation function,  $A_{\text{osc}} \cos(2\pi f_{\text{osc}} t + \varphi) e^{-t/\tau_{\text{damping}}}$ ,

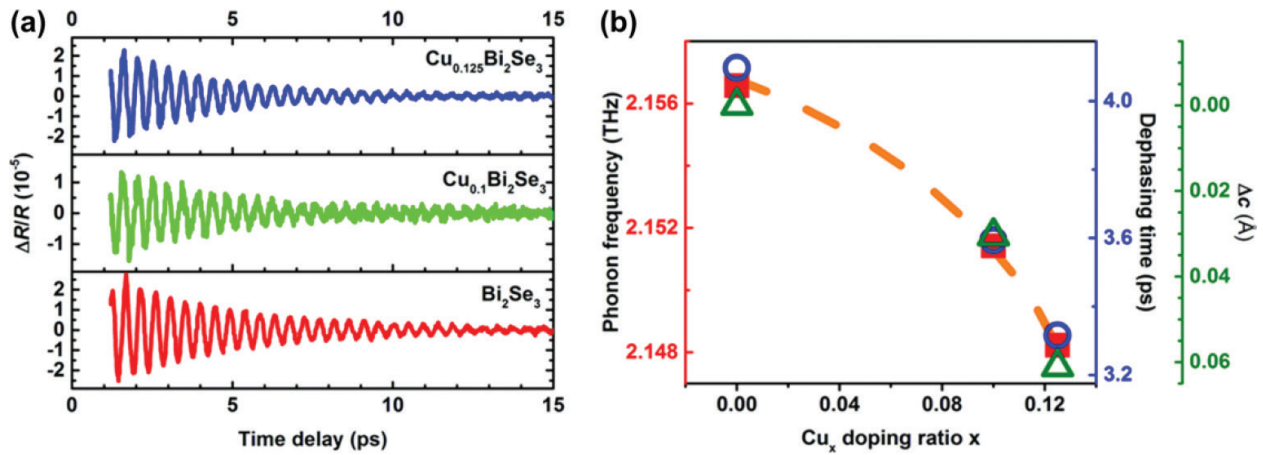


**Figure 8.** (a) High-frequency temporal variations of  $\Delta R/R$  signals for  $\text{Cu}_x\text{Bi}_2\text{Se}_3$  ( $x = 0, 0.1, 0.125$ ) crystals extracted from Figure 7(b). (b) Phonon frequency (red squares), dephasing time of  $A_{1g}^{-1}$  phonon mode (blue circles) and changes in lattice constant of  $c$ -axis (green triangles) in  $\text{Cu}_x\text{Bi}_2\text{Se}_3$  crystals as a function of Cu doping concentrations.

was used to fit the original data in **Figure 8(a)** to get the dephasing time ( $\tau_{\text{dephasing}}$ ) and the phonon frequency ( $f_{\text{osc}}$ ) for the  $\text{Cu}_x\text{Bi}_2\text{Se}_3$  crystals. As shown in **Figure 8(b)**, both dephasing time and phonon frequency shrink as Cu concentrations increase ( $x$ ). This indicates that an additional Cu atom deforms the Se-Bi-Se-Bi-Se chain in  $\text{Cu}_x\text{Bi}_2\text{Se}_3$  crystals. Furthermore, the lattice constant of  $c$ -axis increases slightly with increasing Cu concentrations [**Figure 8(b)**], implying that the QL chain in  $\text{Cu}_x\text{Bi}_2\text{Se}_3$  is stretched by introducing Cu atoms. Thus, the scenario of stretching the QL chain length is that the Cu atoms (form a mediated layer) are intercalated between QLs to strengthen the interaction between QLs. Moreover, the QLs are further deformed by these intercalated Cu atoms.

### 4.3. Intradband relaxations in topological insulators

The femtosecond snapshots of the relaxation processes and Dirac fermion-phonon coupling strength of 3D TI  $\text{Bi}_2\text{Se}_3$  were revealed by OPMP spectroscopy [26]. In this study, several selected  $\text{Bi}_2\text{Se}_3$  single crystals with a wide range of carrier concentrations ( $n$ ) from  $51.5 \times 10^{18}$  to  $0.25 \times 10^{18} \text{ cm}^{-3}$  were studied. **Table 1** summarizes the doping levels of samples (#1:  $n = 51.5 \times 10^{18} \text{ cm}^{-3}$ , #2:

Code	$E_F - E_{\text{Dirac point}}$ (meV)	Carrier concentration		$n_{\text{surface}} / (n_{\text{surface}} + n_{\text{bulk}} \cdot d)$
		$n_{\text{bulk}}$ ( $10^{18} \text{ cm}^{-3}$ )	$n_{\text{surface}}$ ( $10^{13} \text{ cm}^{-2}$ )	
#1	422	$-51.5 \pm 0.84$	-1.45	0.11
#2	325	$-13.9 \pm 0.26$	-0.83	0.20
#3	284	$-5.58 \pm 0.25$	-0.72	0.35
#4	260	$-0.25 \pm 0.01$	-0.47	0.89

**Table 1.** Fermi energy and carrier concentrations of bulk and surface states of various  $\text{Bi}_2\text{Se}_3$  single crystals. All samples are  $n$ -type. “ $d = 23.5 \text{ nm}$ ” is the penetration depth of 800 nm pumping light.

$n = 13.9 \times 10^{18} \text{ cm}^{-3}$ , #3:  $n = 5.58 \times 10^{18} \text{ cm}^{-3}$ , and #4:  $n = 0.25 \times 10^{18} \text{ cm}^{-3}$ ). The OPMP spectra and the corresponding ARPES images of the samples are shown in **Figure 9(a)** and **(b)** [26]. The OPMP spectra clearly show a positive  $\Delta R/R$  peak for high  $n \geq 13.9 \times 10^{18} \text{ cm}^{-3}$  ( $\text{Bi}_2\text{Se}_3$  #1 and #2). In contrast, this positive peak gradually diminishes as  $n$  decreases, while an additional negative peak appears for the cases of  $n = 5.58 \times 10^{18} \text{ cm}^{-3}$  and  $n = 0.25 \times 10^{18} \text{ cm}^{-3}$ .

Based on the ARPES image and the energy band structure of TI  $\text{Bi}_2\text{Se}_3$ , a model is proposed [in **Figure 10(a)**] for the optical pumping (1.55 eV) and mid-infrared probing processes to elucidate the origins of both positive and negative signals. The band gap of  $\text{Bi}_2\text{Se}_3$  is  $\sim 300 \text{ meV}$ , as shown in the ARPES images of **Figure 9(b)**, which is much larger than the probe photon energy (87~153 meV) of the mid-infrared (mid-IR). Thus, it does not allow the occurring of the interband transitions between the valence band (VB) and the conduction band (CB) of the bulk. Meanwhile, the free-carrier absorption in the CB [the probe (1) in **Figure 10(a)**] and Dirac cone surface state [the probe (2) in **Figure 10(a)**] will dominate the probe processes, which can be assigned to the positive and negative peaks in  $\Delta R/R$ , respectively. To reveal the physical meanings of the positive peak in  $\Delta R/R$ , the photon energy dependence of  $\Delta R/R$  for #1

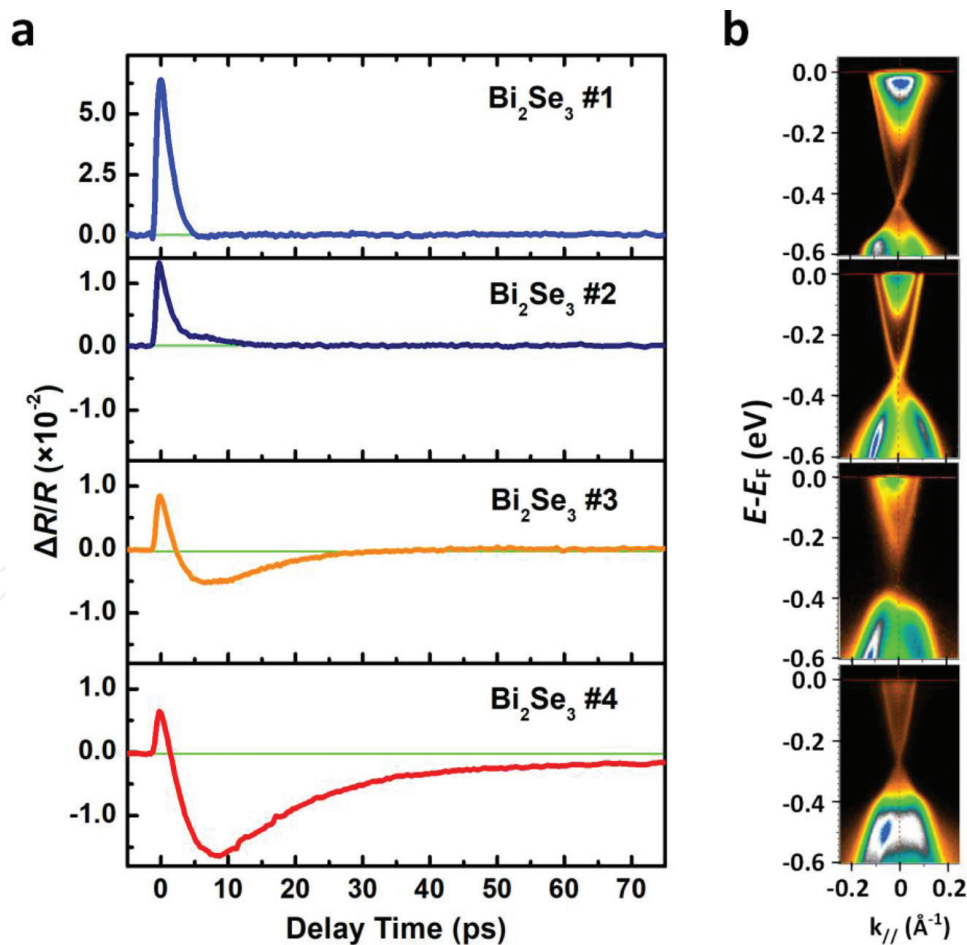


**Figure 9.** Carrier concentration ( $n$ ) dependence of the transient changes in reflectivity  $\Delta R/R$  in  $\text{Bi}_2\text{Se}_3$  single crystals. (a)  $\Delta R/R$  of samples #1 ( $n = 51.5 \times 10^{18} \text{ cm}^{-3}$ ), #2 ( $n = 13.9 \times 10^{18} \text{ cm}^{-3}$ ), #3 ( $n = 5.58 \times 10^{18} \text{ cm}^{-3}$ ), and #4 ( $n = 0.25 \times 10^{18} \text{ cm}^{-3}$ ) with a fluence of  $34 \mu\text{J}/\text{cm}^2$  for pumping and a photon energy of 141 meV for probing. (b) ARPES images on samples of (a) [26].

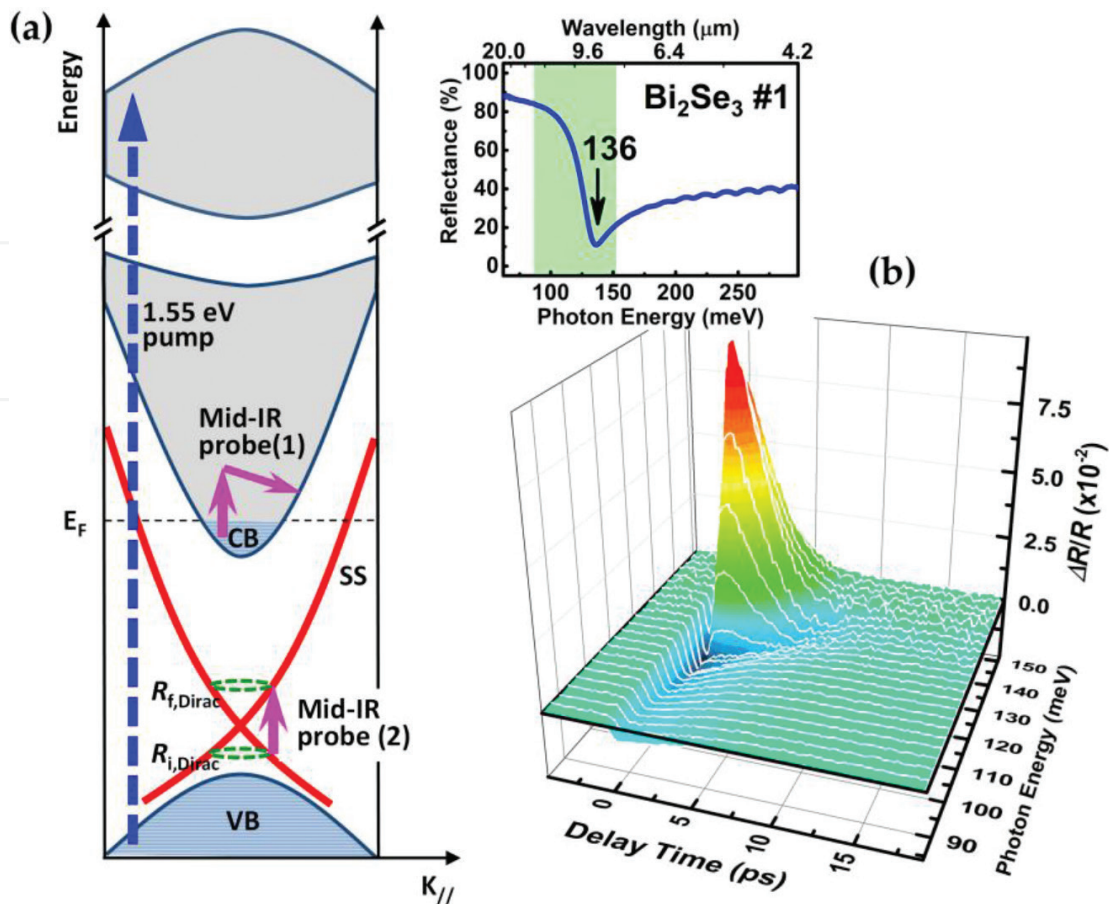


**Figure 10.** Schematic energy band structure and photon energy-dependent  $\Delta R/R$  in a bulk state. (a) Schematic band structure of TIs based on the ARPES images in Figure 9(b) and the pump-probe processes. CB: Conduction band, VB: Valence band, SS: Surface state.  $R_{i,Dirac}$  &  $R_{f,Dirac}$ : The circumferences of initial/final states in Dirac cone for probing. (b) With a fluence of  $38 \mu\text{J}/\text{cm}^2$  for pumping, the  $\Delta R/R$  of  $\text{Bi}_2\text{Se}_3$  #1 at various photon energies (wavenumber) from 87 to 153 meV ( $700\text{--}1234 \text{ cm}^{-1}$ ). Inset: The Fourier transform infrared (FTIR) reflectance spectrum of  $\text{Bi}_2\text{Se}_3$  #1. The gray area indicates the range of the mid-IR photon energy used in this study [26].

sample is studied and shown in **Figure 10(b)**. Clearly,  $\Delta R/R$  gradually changes from positive to negative as decreasing the photon energy. At around 136 meV ( $1100 \text{ cm}^{-1}$ ), it appears that intermediate signals mixed with both positive and negative peaks, corresponding to deep in the Fourier transform infrared (FTIR) reflectance spectrum [the inset of **Figure 10(b)**]. The excited carriers after pumping suffer the so-called intervalley scattering, leading to the red shift of the reflectance spectra. Thus, the reflectivity increases as a function of time when probing photon energy is higher than the position of the 136 meV deep. In contrast, the reflectivity decreases as a function of time when probing photon energy is smaller than the 136 meV deep. Similar results were also observed in a typical semiconductor n-type GaAs [23].

As found in **Figure 9** and **Table 1**, the amplitude of positive peak in  $\Delta R/R$  gradually decreases as bulk carrier concentrations reduce. Meanwhile, the negative peak of  $\Delta R/R$  increases while reducing the bulk and surface carrier concentrations. Intriguingly, the negative peak increases substantially with an increasing ratio of the surface to total carrier concentration  $[n_{\text{surface}}/(n_{\text{surface}} + n_{\text{bulk}} \cdot d)]$  in **Table 1**, implying a close relation between the negative peak of  $\Delta R/R$  and Dirac fermions. In

addition, **Figure 11(a)** shows the  $\Delta R/R$  signal as a function of the pumping fluences. The positive peak exhibits a stronger dependence on the pumping fluences than the negative peak does. For a pumping fluence of  $3.3 \mu\text{J}/\text{cm}^2$ , the maximum photo-induced carrier density  $\Delta n$  is around  $2.54 \times 10^{18} \text{ cm}^{-3}$ . Indeed, if one absorbed photon generates one photo-induced carrier, the maximum photo-induced carrier density can be estimated by  $\Delta n = (1-R) \times F / (E \times \delta)$ , where  $R = 0.55$  is the reflectance,  $F = 3.3 \mu\text{J}/\text{cm}^2$  is pumping fluence,  $E = 2.48 \times 10^{-19} \text{ J}$  ( $= 1.55 \text{ eV}$ ) is the pumping photon energy,  $\delta = 23.5 \text{ nm}$  is the penetration depth. Consequently, the negative peak still subsists at the low pumping fluence of  $3.3 \mu\text{J}/\text{cm}^2$ , while the positive peak almost vanishes [see **Figure 11(b)**]. Namely, the process (1) associated with the positive peak can be suppressed and the process (2) associated with the negative peak can be preserved by reducing the pumping fluences. To quantitatively certify the relation between the negative peak and Dirac fermions, the amplitude of the negative peak dependence of probing photon energy is studied using low  $n$  samples #3 and #4 to avoid disturbance of the positive peak [**Figure 11(b)**]. According to Fermi's golden rule, the amplitude of the negative peak should be proportional to the transition probability ( $T_{i \rightarrow f}$ ) between the

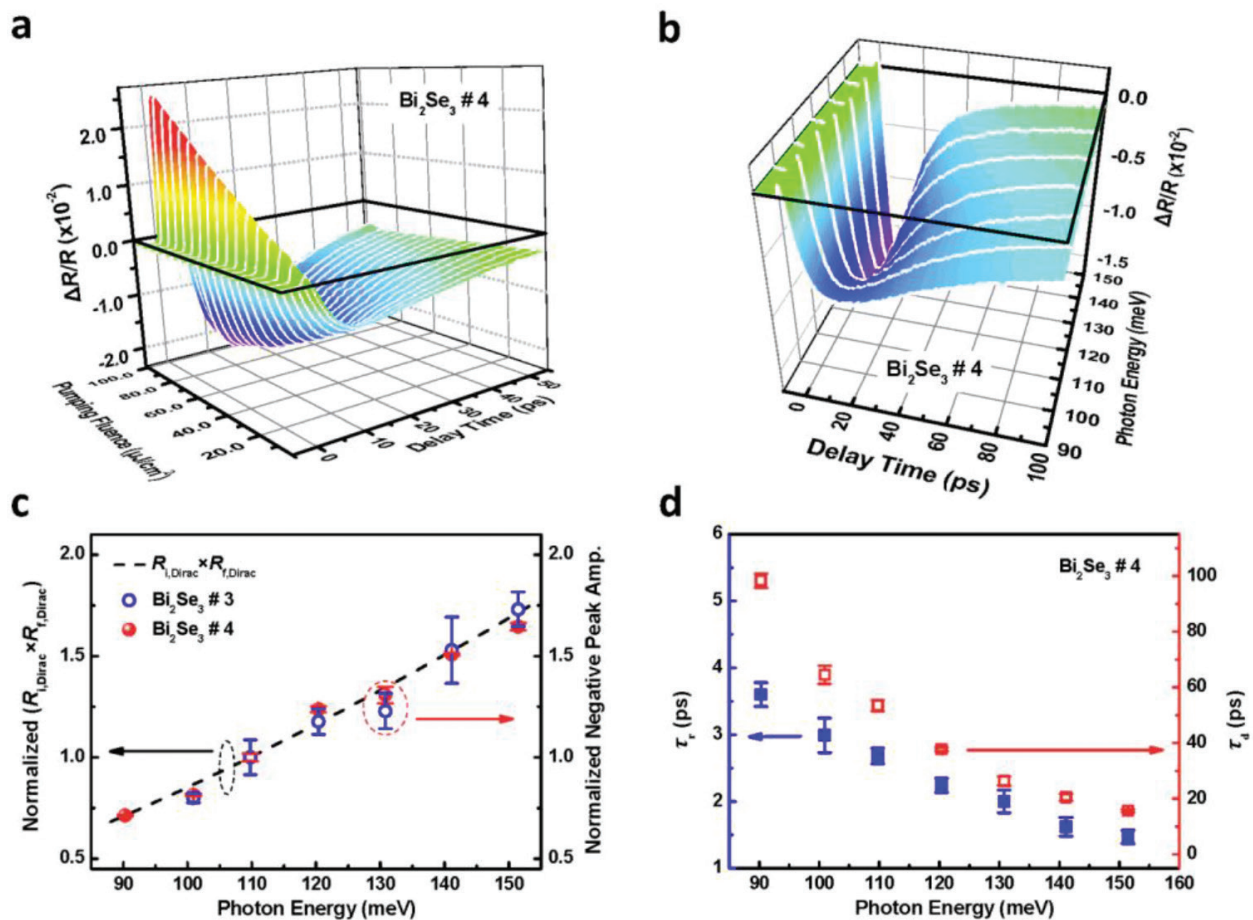


**Figure 11.** Pumping fluence and photon energy dependence of  $\Delta R/R$  and its amplitude and rising (decay) time in the surface state. (a) With probing photon energy of 141 meV, the  $\Delta R/R$  of  $\text{Bi}_2\text{Se}_3$  #4 at various pumping fluences from 3.3 to  $105 \mu\text{J}/\text{cm}^2$ . (b) With pumping fluence of  $3.3 \mu\text{J}/\text{cm}^2$ , the  $\Delta R/R$  of  $\text{Bi}_2\text{Se}_3$  #4 at various photon energies from 90 to 152 meV. (c) The photon energy dependence of negative peak amplitude of  $\Delta R/R$  in (b). The photon energy-dependent normalized absorption probability [dashed line, i.e.  $R_{1,\text{Dirac}} \times R_{1,\text{Dirac}}$  in **Figure 10 (a)**] of the mid-IR probe beam in the Dirac cone. (d) The photon energy dependence of the rising time ( $\tau_r$ ) and decay time ( $\tau_d$ ) of  $\Delta R/R$  in (b) [26].

initial and final density of states in the Dirac cone. Indeed, in **Figure 11(c)**, the  $R_{i,Dirac} \times R_{f,Dirac}$  presents linear relation with probing photon energy, reflecting the proportional relation to the transition rate between the initial and final density of states for the mid-IR probe process (2) in the Dirac cone [**Figure 10(a)**]. This confirms that the negative peak of  $\Delta R/R$  is predominantly attributed to the mid-IR probe process (2) in the Dirac cone. Consequently, the ultrafast dynamics of the Dirac fermions can be clearly disclosed by the negative peak of  $\Delta R/R$ .

As shown in **Figure 11(d)**, both rising time ( $\tau_r$ ) and decay time ( $\tau_d$ ) of the negative peak of  $\Delta R/R$  strongly depend on the probing photon energy. The  $\tau_r$  becomes longer when the probed regime is closer to the Dirac point (or smaller probing energy). The ultrafast relaxation picture for Dirac fermions in TIs can be established. The major process right after the 1.55 eV pumping is that the carriers in the bulk valence band (BVB) are excited to the bulk conduction band (BCB). The carrier recombination between the BCB and BVB can be ignored in this study because of the large timescale (typically  $\gg 1$  ns) for such a process. Consequently, the unoccupied states in BVB would mainly be refilled by carriers in the upper Dirac cone. Carriers in the Dirac cone can be easily transferred into the unoccupied states in BVB due to the overlapping between the Dirac cone and BVB [see **Figure 9(b)**], leading to the increase in the number of the unoccupied states near the Dirac point and thus enhancing the absorption channel for process (2) in the Dirac cone [**Figure 10(a)**]. Therefore, the reflectivity of the mid-IR probing light decreases within 1.47~3.60 ps, that is, the rising time of the negative peak in **Figure 11(b)** and **(d)**. Once the carriers in the Dirac cone relax into BVB, the excited carriers in the BCB are subsequently injected into the unoccupied states in the Dirac cone to diminish the absorption channel for the mid-IR process (2) [**Figure 10(a)**] and consequently lead to the increased mid-IR reflectivity within 14.8~87.2 ps. The timescale ( $\tau_d$ ) of this process is several tens of picoseconds, which is much longer than the  $\tau_r$  of several picoseconds, because the carriers in BCB cannot directly transfer into the top of the Dirac cone without overlaps occurring between them and other auxiliaries, for example, phonons.

The relaxation of Dirac fermions has been demonstrated via phonon medium [38, 39]. The coupling strength ( $\lambda$ ) between Dirac fermions and phonons varies at different positions of the Dirac cone, which can be revealed from the photon energy-dependent rising time. Based on the second moment of the Eliashberg function [40], the coupling strength ( $\lambda$ ) is inversely proportional to the relaxation time ( $\tau_e$ ) of excited electrons:

$$\lambda \langle \omega^2 \rangle \propto \frac{1}{\tau_e} \quad (2)$$

where  $\omega$  is the phonon energy which couples with the electrons. For the estimate of  $\langle \omega^2 \rangle$ , some vibrational modes are more efficiently coupled to Dirac fermions than the others. For  $\text{Bi}_2\text{Se}_3$ , the symmetric  $A_{1g}^1$  mode of ~8.9 meV is coherently excited by photoexcitation and efficiently coupled. Taking  $\tau_e = \tau_r$  in **Figure 11(d)** and  $T_e = 370$  K (obtained from [32] at the aforementioned low pumping fluence) to estimate the coefficient of  $(\pi k_B T_e / 3\hbar)$  in Eq. (2), photon energy dependence of the Dirac fermion-phonon coupling strength is  $\lambda = 0.08\text{--}0.19$ . The Dirac fermion-phonon coupling strength measured by the present OPMP becomes significantly smaller near the Dirac point (the point of  $K_{\parallel}=0$ ). As getting closer to the Dirac point, Dirac

fermions will possess a weaker coupling with the phonons to reduce the scatterings with phonons. In addition, the effective mass of Dirac fermions in the surface state gradually decreases when approaching the Dirac point, which is consistent with the results in graphene [9].

## 5. Conclusion

We report the ultrafast dynamics of carriers and phonons in topological insulator  $\text{Bi}_2\text{Se}_3$ ,  $\text{Cu}_x\text{Bi}_2\text{Se}_3$  ( $x = 0, 0.1, 0.125$ ) single crystals. By time-resolved pump-probe spectroscopy, one damped fast oscillation was clearly observed in the transient reflectivity changes ( $\Delta R/R$ ) for  $\text{Cu}_x\text{Bi}_2\text{Se}_3$ , which is assigned to the coherent optical phonon ( $A_{1g}^1$ ). The frequency of  $A_{1g}^1$  phonon decreases considerably with increasing Cu contents, suggesting the intercalation of Cu atoms between quintuple layers of  $\text{Bi}_2\text{Se}_3$ . The schematic illustration of the direct transitions and subsequent relaxation processes induced by optical excitation in  $\text{Bi}_2\text{Se}_3$  single crystals is also reported here. The femtosecond snapshots of the relaxation processes were revealed by optical pump and mid-infrared probe spectroscopy. Especially, the Dirac fermion dynamics in the Dirac cone surface state near the Dirac point of  $\text{Bi}_2\text{Se}_3$  was unambiguously revealed through the negative peak of  $\Delta R/R$ . The Dirac fermion-phonon coupling strength was found in range of 0.08–0.19 and the strength is reduced as getting closer to the Dirac point. These results are extremely crucial to the design of Dirac fermion devices and optoelectronics, especially in the mid-IR and THz ranges.

## Acknowledgements

Financial support from Vietnam National Foundation for Science and Technology Development (NAFOSTED) under grant number 103.99–2015.17, the Ministry of Science and Technology of the Republic of China, Taiwan (Grant No. 103-2628-M-009-002-MY3, 103-2119-M-009-004-MY3, 106-2119-M-009-013-FS, 106-2628-M-009-003-MY3) and the Grant MOE ATU Program at NCTU are gratefully acknowledged.

## Author details

Phuoc Huu Le<sup>1\*</sup> and Chih-Wei Luo<sup>2,3\*</sup>

\*Address all correspondence to: lhuophuoc@ctump.edu.vn and cwluo@mail.nctu.edu.tw

1 Faculty of Basic Sciences, Can Tho University of Medicine and Pharmacy, Can Tho, Vietnam

2 Department of Electrophysics, National Chiao Tung University, Hsinchu, Taiwan

3 Taiwan Consortium of Emergent Crystalline Materials, Ministry of Science and Technology, Taipei, Taiwan

## References

- [1] Fu L, Kane CL, Mele EJ. Topological insulators in three dimensions. *Physical Review Letters*. 2007;**98**:106803. DOI: 10.1103/PhysRevLett.98.106803
- [2] Moore JE, Balents L. Topological invariants of time-reversal-invariant band structures. *Physical Review B*. 2007;**75**:121306(R). DOI: 10.1103/PhysRevB.75.121306
- [3] Hsieh D, Qian D, Wray L, Xia Y, Hor YS, Cava RJ, Hasan MZ. A topological Dirac insulator in a quantum spin hall phase. *Nature*. 2008;**452**:970-974. DOI: 10.1038/nature06843
- [4] Hsieh D, Xia Y, Qian D, Wray L, Meier F, Dil JH, Osterwalder J, Patthey L, Fedorov AV, Lin H, Bansil A, Grauer D, Hor YS, Cava RJ, Hasan MZ. Observation of time-reversal-protected single-Dirac-cone topological-insulator states in  $\text{Bi}_2\text{Te}_3$  and  $\text{Sb}_2\text{Te}_3$ . *Physical Review Letters*. 2009;**103**:146401. DOI: 10.1103/PhysRevLett.103.146401
- [5] Moore JE. The birth of topological insulators. *Nature*. 2010;**464**:194-198. DOI: 10.1038/nature08916
- [6] Hasan MZ, Kane CL. Colloquium: Topological insulators. *Reviews of Modern Physics*. 2010;**82**:3045-3067. DOI: 10.1103/RevModPhys.82.3045
- [7] Hasan MZ, Moore JE. Three-dimensional topological insulators. *Annual Review of Condensed Matter Physics*. 2011;**2**:55-78. DOI: 10.1146/annurev-conmatphys-062910-140432
- [8] Qi X-L, Zhang S-C. Topological insulators and superconductors. *Reviews of Modern Physics*. 2011;**83**:1057-1110. DOI: 10.1103/RevModPhys.83.1057
- [9] Novoselov KS, Geim AK, Morozov SV, Jiang D, Katsnelson MI, Grigorieva IV, Dubonos SV, Firsov AA. Two-dimensional gas of massless Dirac fermions in graphene. *Nature*. 2005;**438**:197-200. DOI: 10.1038/nature04233
- [10] Coleman JN, Lotya M, O'Neill A, Bergin SD, King PJ, Khan U, Young K, Gaucher A, De S, Smith RJ, Shvets IV, Arora SK, Stanton G, Kim H-Y, Lee K, Kim GT, Duesberg GS, Hallam T, Boland JJ, Wang JJ, Donegan JF, Grunlan JC, Moriarty G, Shmeliov A, Nicholls RJ, Perkins JM, Grievson EM, Theuwissen K, McComb DW, Nellist PD, Nicolosi V. Two-dimensional nanosheets produced by liquid exfoliation of layered materials. *Science*. 2011;**331**:568-571. DOI: 10.1126/science.1194975
- [11] Xue Q-K. Nanoelectronics: A topological twist for transistors. *Nature Nanotechnology*. 2011;**6**:197-198. DOI: 10.1038/nnano.2011.47
- [12] Le PH, Liao C-N, Luo CW, Lin J-Y, Leu J. Thermoelectric properties of nanostructured bismuth-telluride thin films grown using pulsed laser deposition. *Journal of Alloy Compound*. 2014;**615**:546-552. DOI: 10.1016/j.jallcom.2014.07.018
- [13] Le PH, Liao C-N, Luo CW, Lin J-Y, Leu J. Thermoelectric properties of bismuth-selenide films with controlled morphology and texture grown using pulsed laser deposition. *Applied Surface Science*. 2013;**285P**:657-663. DOI: 10.1016/j.apsusc.2013.08.107

- [14] Tuyen LTC, Le PH, Luo CW, Leu J. Thermoelectric properties of nanocrystalline  $\text{Bi}_3\text{Se}_2\text{Te}$  thin films grown using pulsed laser deposition. *Journal of Alloys and Compounds*. 2016;**673**:107-114. DOI: 10.1016/j.jallcom.2016.03.006
- [15] Zhang H, Liu C-X, Qi X-L, Dai X, Fang Z, Zhang S-C. Topological insulators in  $\text{Bi}_2\text{Se}_3$ ,  $\text{Bi}_2\text{Te}_3$  and  $\text{Sb}_2\text{Te}_3$  with a single Dirac cone on the surface. *Nature Physics*. 2009;**5**:438-442. DOI: 10.1038/NPHYS1270
- [16] Le PH, Tzeng W-Y, Chen H-J, Luo CW, Lin J-Y, Leu J. Superconductivity in textured bi clusters/ $\text{Bi}_2\text{Te}_3$  films. *APL Mater*. 2014;**2**:096105. DOI: 10.1063/1.4894779
- [17] Le PH, Chiu S-P, Jian SR, Luo CW, Lin J-Y, Lin J-J, Wu KH, Gospodinov M. Nanomechanical, structural, and transport properties of  $\text{Bi}_3\text{Se}_2\text{Te}$  thin films. *Journal of Alloys and Compounds*. 2016;**679**:350-357. DOI: 10.1016/j.jallcom.2016.03.226
- [18] Le PH, Liu P-T, Luo CW, Lin J-Y, Wu KH. Thickness-dependent magnetotransport properties and terahertz response of topological insulator  $\text{Bi}_2\text{Te}_3$  thin films. *Journal of Alloys and Compounds*. 2017;**692**:972-979. DOI: 10.1016/j.jallcom.2016.09.109
- [19] Miller GR, Li C-Y, Spencer CW. Properties of  $\text{Bi}_2\text{Te}_3$ -  $\text{Bi}_2\text{Se}_3$  alloys. *Journal of Applied Physics*. 1963;**34**:1398. DOI: 10.1063/1.1729588
- [20] Xia Y, Qian D, Hsieh D, Wray L, Pal A, Lin H, Bansil A, Grauer D, Hor YS, Cava RJ, Hasan MZ. Observation of a large-gap topological-insulator class with a single Dirac cone on the surface. *Nature Physics*. 2009;**5**:398-402. DOI: 10.1038/NPHYS1274
- [21] Moss TS, Hawkins TDF, Burrell GJ. Use of plasma edge reflection measurements in the study of semiconductors. *Journal of Physics C*. 1968;**1**:1435-1446. DOI: 10.1088/0022-3719/1/5/333
- [22] Choi HS, Ahn JS, Jung JH, Noh TW, Kim DH. Mid-infrared properties of a  $\text{VO}_2$  film near the metal-insulator transition. *Physical Review B. Condensed Matter*. 1996;**54**:4621-4628. DOI: 10.1103/PhysRevB.54.4621
- [23] Dantzig NAV, Planken PCM. Time-resolved far-infrared reflectance of n-type GaAs. *Physical Review B*. 1999;**59**:1586. DOI: 10.1103/PhysRevB.59.1586
- [24] Nagai M, Shimano R, Kuwata-Gonokami M. Electron-hole droplet formation in direct-gap semiconductors observed by mid-infrared pump-probe spectroscopy. *Physical Review Letters*. 2001;**86**:5795-5798. DOI: 10.1103/PhysRevLett.86.5795
- [25] Winnerl S, Orlita M, Plochocka P, Kossacki P, Potemski M, Winzer T, Malic E, Knorr A, Sprinkle M, Berger C, de Heer WA, Schneider H, Helm M. Carrier relaxation in epitaxial graphene photoexcited near the Dirac point. *Physical Review Letters*. 2011;**107**:237401. DOI: 10.1103/PhysRevLett.107.237401
- [26] Luo CW, Wang HJ, Ku SA, Chen H-J, Yeh TT, Lin J-Y, Wu KH, Juang JY, Young BL, Kobayashi T, Cheng C-M, Chen C-H, Tsuei K-D, Sankar R, Chou FC, Kokh KA, Tereshchenko OE, Chulkov EV, Andreev YM, Gu GD. Snapshots of Dirac fermions near the Dirac point in topological insulators. *Nano Letters*. 2013;**13**:5797-5802. DOI: 10.1021/nl4021842

- [27] Kaindl RA, Woerner M, Elsaesser T, Smith DC, Ryan JF, Farnan GA, McCurry MP, Walmsley DG. Ultrafast mid-infrared response of  $\text{YBa}_2\text{Cu}_3\text{O}_7$ . *Science*. 2000;**287**:470-473. DOI: 10.1126/science.287.5452.470
- [28] Luo CW, Tseng PS, Chen H-J, Wu KH, Li LJ. Dirac fermion relaxation and energy loss rate near the Fermi surface in monolayer and multilayer graphene. *Nanoscale*. 2014;**6**:8575-8578. DOI: 10.1039/c4nr02205j
- [29] Hajlaoui M, Papalazarou E, Mauchain J, Lantz G, Moisan N, Boschetto D, Jiang Z, Miotkowski I, Chen YP, Taleb-Ibrahimi A, Perfetti L, Marsi M. Ultrafast surface carrier dynamics in the topological insulator  $\text{Bi}_2\text{Te}_3$ . *Nano Letters*. 2012;**12**:3532-3536. DOI: 10.1021/nl301035x
- [30] Crepaldi A, Ressel B, Cilento F, Zacchigna M, Grazioli C, Berger H, Bugnon P, Kern K, Grioni M, Parmigiani F. Ultrafast photodoping and effective Fermi-Dirac distribution of the Dirac particles in  $\text{Bi}_2\text{Se}_3$ . *Physical Review B*. 2012;**86**:205133. DOI: 10.1103/PhysRevB.86.205133
- [31] Sobota JA, Yang S, Analytis JG, Chen YL, Fisher IR, Kirchmann PS, Shen Z-X. Ultrafast optical excitation of a persistent surface-state population in the topological insulator  $\text{Bi}_2\text{Se}_3$ . *Physical Review Letters*. 2012;**108**:117403. DOI: 10.1103/PhysRevLett.108.117403
- [32] Wang YH, Hsieh D, Sie EJ, Steinberg H, Gardner DR, Lee YS, Jarillo-Herrero P, Gedik N. Measurement of intrinsic Dirac fermion cooling on the surface of the topological insulator  $\text{Bi}_2\text{Se}_3$  using time-resolved and angle-resolved photoemission spectroscopy. *Physical Review Letters*. 2012;**109**:127401. DOI: 10.1103/PhysRevLett.109.127401
- [33] Chen H-J, Wu KH, Luo CW, Uen TM, Juang JY, Lin J-Y, Kobayashi T, Yang H-D, Sankar R, Chou FC, Berger H, Liu JM. Phonon dynamics in  $\text{Cu}_x\text{Bi}_2\text{Se}_3$  ( $x = 0, 0.1, 0.125$ ) and  $\text{Bi}_2\text{Se}_2$  crystals studied using femtosecond spectroscopy. *Applied Physics Letters*. 2012;**101**:121912. DOI: 10.1063/1.4754005
- [34] Othonos A. Probing ultrafast carrier and phonon dynamics in semiconductors. *Journal of Applied Physics*. 1998;**83**:1789. DOI: 10.1063/1.367411
- [35] Kumar N, Ruzicka BA, Butch NP, Syers P, Kirshenbaum K, Paglione J, Zhao H. Spatially resolved femtosecond pump-probe study of topological insulator  $\text{Bi}_2\text{Se}_3$ . *Physical Review B*. 2011;**83**:235306. DOI: 10.1103/PhysRevB.83.235306
- [36] Zhang J, Peng Z, Soni A, Zhao Y, Xiong Y, Peng B, Wang J, Dresselhaus MS, Xiong Q. Raman spectroscopy of few-quintuple layer topological insulator  $\text{Bi}_2\text{Se}_3$  nanoplatelets. *Nano Letters*. 2011;**11**:2407-2414. DOI: 10.1021/nl200773n
- [37] Richter W, Köhler H, Becker CR. A Raman and far-infrared investigation of phonons in the rhombohedral V2-V13 compounds. *Physica Status Solidi*. 1977;**84**:619-628
- [38] Zhu X, Santos L, Howard C, Sankar R, Chou FC, Chamon C, El-Batanouny M. Electron-phonon coupling on the surface of the topological insulator  $\text{Bi}_2\text{Se}_3$  determined from surface-phonon dispersion measurements. *Physical Review Letters*. 2012;**108**:185501. DOI: 10.1103/PhysRevLett.108.185501

- [39] Pan Z-H, Fedorov AV, Gardner D, Lee YS, Chu S, Valla T. Measurement of an exceptionally weak electron-phonon coupling on the surface of the topological insulator  $\text{Bi}_2\text{Se}_3$  using angle-resolved photoemission spectroscopy. *Physical Review Letters*. 2012;**108**:187001. DOI: 10.1103/PhysRevLett.108.187001
- [40] Allen PB. Theory of thermal relaxation of electrons in metals. *Physical Review Letters*. 1987;**59**:1460. DOI: 10.1103/PhysRevLett.59.1460

IntechOpen

IntechOpen

